Earth, Planets and Space
a SpringerOpen Journal

LETTER Open Access

Three-dimensional electromagnetic imaging of fluids and melts beneath the NE Japan arc revisited by using geomagnetic transfer function data

Wataru Kanda* and Yasuo Ogawa

Abstract

The three-dimensional distribution of fluids and melts under the NE Japan arc was imaged using its resistivity structure, modeled with geomagnetic transfer functions. The data were collected at 37 stations located on a 20-km grid, at periods ranging from 16 to 256 s. In spite of the narrow period band nature, these periods turn out to be sensitive to conductors in the deep crust and upper mantle. The geomagnetic transfer functions represent lateral resistivity variations, which yield inherently nonunique model results when using the geomagnetic transfer functions alone. However, by fixing the resistivity structure of the surrounding seawater distribution, the intrinsic nonuniqueness is alleviated. In this study, we show an inversion result using a 100-Ωm uniform Earth with fixed resistivity of surrounding oceans. As a result, it was found that the features of the short period transfer function require shallow conductors in the upper crust, which is suggested to represent the northern Tohoku conducting belt of a previous study. The final model is characterized by a highly conductive zone along the quaternary volcanic arc in the depth range of the lower crust to the upper mantle. The conductor, which is obtained mainly from the features of longer-period data, is particularly clear beneath the Sengan geothermal area. The deep crustal conductor implies the existence of partial melt and/or high-salinity fluids.

Keywords: NE Japan; Quaternary volcanoes; Arc magma; 3-D modeling; Electrical resistivity

Findings

Introduction

Geomagnetic transfer functions (TFs) represent the ratio of vertical to horizontal magnetic variations and are robust to the effects of near-surface local anomalies. Pioneering electromagnetic induction studies of the NE Japan region in the 1970s were based on geomagnetic transfer functions (Kato et al. 1971; Honkura 1974; Nishida 1976; Yamashita and Yokoyama 1976; Ogawa et al. 1986). These studies used three-component fluxgate magnetometer data in the period range of 10 min to 2 h to map the undulations of upper mantle conductors.

Kato et al. (1971) modeled the upper mantle conductor in NE Japan, which shallows at the backbone range, using TFs. However, later studies (Yamashita and Yokoyama 1976; Honkura 1974) pointed out that major features of the TFs are influenced by the effects of induced electric currents flowing in the surrounding ocean, including in the Tsugaru Straight between Honshu and Hokkaido islands. On the other hand, in an analysis of the lower crustal conductor to the west of the volcanic front, Ogawa et al. (1986) pointed out, using a two-dimensional (2-D) finite element approach, that the effect of the ocean alone cannot account for the distribution of the TFs at the period of 15 min. A similar conductor was also revealed on the back-arc side of central Japan by using the TFs obtained over four periods each of which ranged from 15 to 120 min (Utada et al. 1986). However, in those studies, the periods of the data used were restricted to a narrow range and the sites were distributed

* Correspondence: kanda@ksvo.titech.ac.jp
Volcanic Fluid Research Center, Tokyo Institute of Technology, 2-12-1 Ookayama, Meguro, Tokyo 152-8551, Japan

along the measurement lines, which led to qualitative interpretations using simplified 2-D forward modeling.

Ogawa (1987a) qualitatively interpreted geomagnetic transfer function data at 37 sites located on a 20 × 20-km grid (as shown in Figure 1) using induction coils in the period range of 16 to 256 s, which was shorter than the periods used in the preceding studies because of the need to clarify the structure of deep crust but was narrow as compared with present-day wideband magnetotelluric measurements (typically 10^{-2} to 10^{4} s). Nonetheless, those periods turned out to be sensitive to the distributions of deep crustal and upper mantle conductive anomalies, as shown below.

Although the sites were distributed on a grid, Ogawa's (1987a) data were still interpreted qualitatively because realistic three-dimensional modeling including the conductive ocean for TF data has long proved difficult. Avdeev et al. (1995) used thin sheet forward modeling to explain the distribution of induction arrows at the period of 16 s and confirmed the existence of crustal conductive anomalies (NTCBs), but they could not fully explain the TFs at longer periods. In this study, we attempted to interpret the TF data quantitatively by use of the three-dimensional (3-D) inversion scheme of Siripunvaraporn and Egbert (2009).

Data

The TF is a complex quantity that is sensitive to the gradient of the conductivity distribution (Rikitake and Yokoyama 1953; Schmucker 1970). When the vertical magnetic field variation (H_z) is expressed as a linear combination of the two horizontal components (H_x and H_y) at a given period T, the TFs (A and B) are defined by the following relationship:

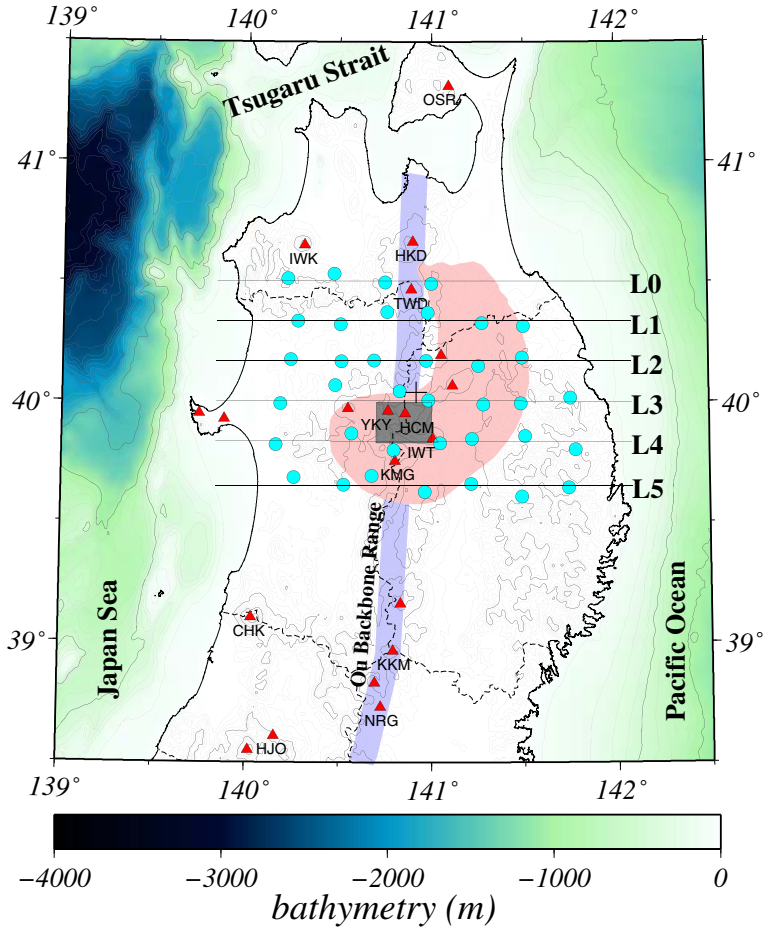

Figure 1 Location map of the sites described in this study. Latitude and longitude are from Ogawa (1987a). The area outlined in pink shows the Northern Tohoku Conducting Belt (NTCB), following Ogawa (1987a). A gray rectangle indicates the Sengan geothermal area. A thick blue line shows the Ou backbone range. Thin horizontal lines (L0 to L5) indicate the locations of cross-sectional profiles shown in later figures. Dashed lines denote prefectural boundaries. Red triangles indicate the locations of major quaternary volcanoes; triangles with three-letter codes denote active volcanoes, as identified by the Japan Meteorological Agency (JMA). OSR, Mt. Osore; IWK, Mt. Iwaki; HKD, Mt. Hakkoda; TWD, Mt. Towada; YKY, Mt. Yakeyama; HCM, Mt. Hachimantai; IWT, Mt. Iwate; KNG, Mt. Komagatake; CHK, Mt. Chokai; KKM, Mt. Kurikoma; NRG, Mt. Narugo; HJO, Mt. Hijiori.

$$H_z(T) = A(T)H_x(T) + B(T)H_y(T) \quad (1)$$

The TF data obtained at 37 sites at three periods (16, 64, and 256 s) are listed in table two of Ogawa (1987a).

For the graphical representation of the TF data, we used the induction arrows of Parkinson's convention (Parkinson 1962), which are shown in Figure 2. It can be considered within an x-y plane that the pair (A, B) of complex coefficients is a vector and that this vector defines the induction arrows. The magnitude and azimuth calculated from the real and imaginary parts of the vector give the length and direction of those arrows, respectively, in which the arrow direction is taken reversely for Parkinson's convention. The real arrows intrinsically tend

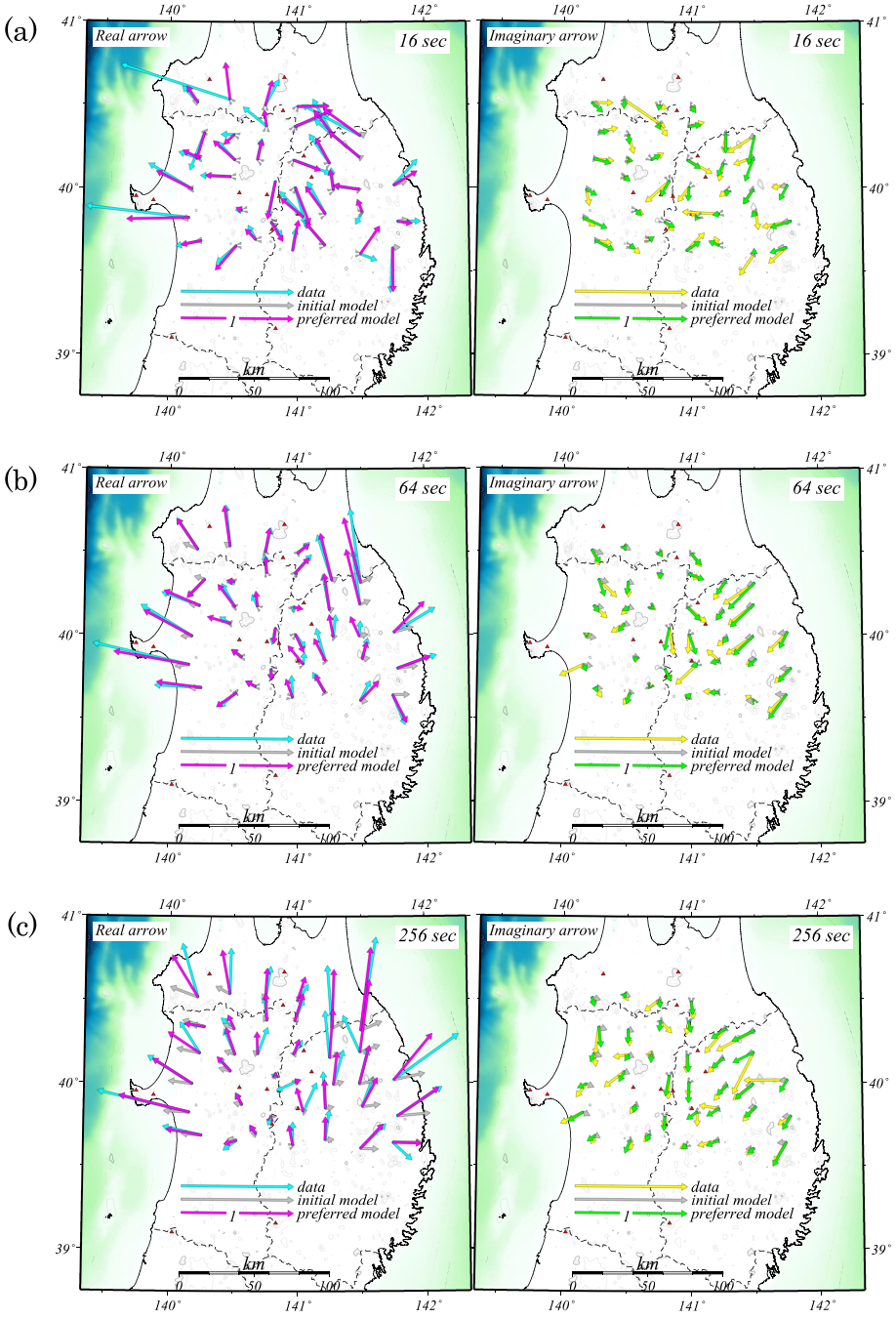

Figure 2 Observed and modeled induction arrows. Induction arrows representing data and calculations from the initial model (Figure 3) and from the inverted model (Figure 4) are drawn at periods of **(a)** 16 s, **(b)** 64 s, and **(c)** 256 s. Real (left) and imaginary (right) arrows are shown in each plot.

to point towards a good conductor (e.g., Simpson and Bahr 2005).

The main features of the distribution of the induction arrows (see Figure 2) and the features of the subsurface structure inferred from those arrows are described in Ogawa (1987a) and are summarized as follows. At a period of 16 s, an upper crustal conductor is suggested by the pairs of induction arrows (red arrows, Figure 2a) at sites east of the volcanic front, which are pointing towards each other, suggesting the existence of a crustal conductor (NTCB, Figure 1). At longer periods, the induction arrows generally show a spatially smoother distribution (Figure 2b,c). Most coastal sites show large real arrows perpendicular to the coastline. The sites on the northernmost profiles (L0 and L1) show large northward components (Figure 2c), but their lengths are shorter near the volcanic front. These data were qualitatively interpreted in terms of conductors along the volcanic front that were reducing the lengths of the northward arrows (Ogawa 1987a).

Methods

We designed finite difference meshes for a 3-D inversion as follows. In the horizontal direction, the core area, centered on the Sengan geothermal area, consisted of a 60 × 60-mesh with a mesh unit length of 4 km. Outside the core area, the mesh size was enlarged by $\sqrt{2}$ times the distance from the core area (Figure 3). In the vertical direction, the minimum mesh length was 10 m at the top layer, with the mesh size gradually increasing with depth. Consequently, the calculation domain of 830 × 830 × 349 km was divided into 78 × 78 × 47 resistivity blocks (Figure 3).

We used TFs at three periods. The error of the TFs was estimated by Ogawa (1987a) as the 95% confidence limit under the assumption of F-distributed data. For the 3-D modeling, we approximated the standard deviation of the TF as half of the TF errors, which are listed in Ogawa (1987a). An error floor of 5% was used for the inversion.

The inversion using the TF data alone has an inherent ambiguity and a resistivity structure that cannot be recovered uniquely unless a proper starting model is given

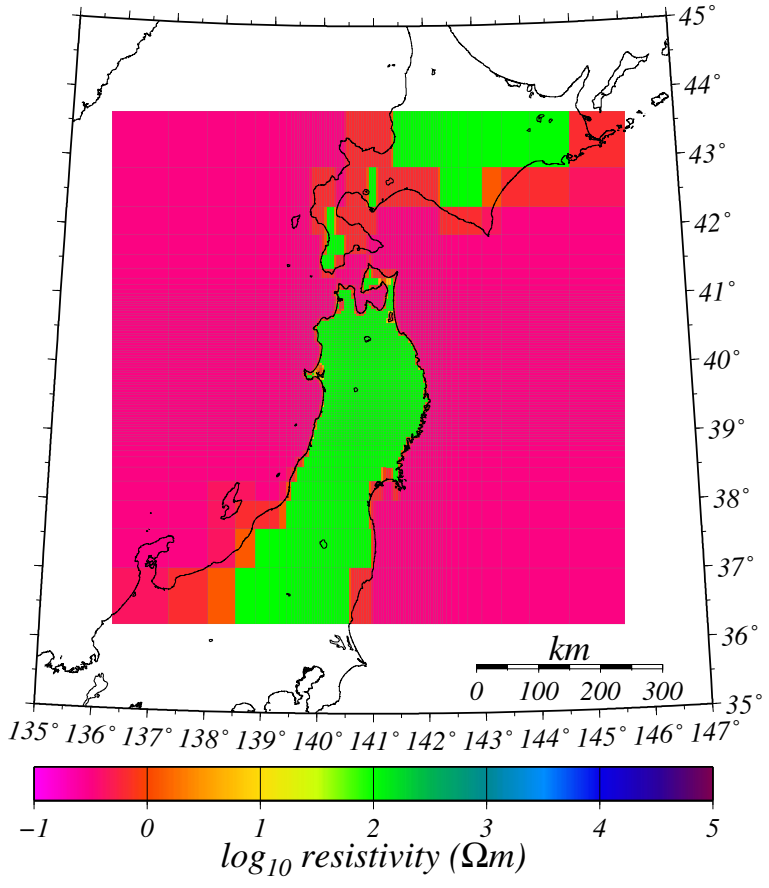

Figure 3 Initial model of the 3-D inversion. The resistivity structure of the Earth was a uniform-half space with a resistivity of 100 Ωm; resistivity blocks corresponding to seawater were fixed at 0.33 Ωm. Resistivities of blocks containing the land-sea boundary were given as the weighted mean of two values, according to the volume ratio.

(Siripunvaraporn and Egbert 2009). In this study, the initial model consisted of a 100-Ωm uniform Earth and surrounding seawater of 0.33 Ωm distributed over known bathymetry. Blocks containing both seawater and land were fixed at a resistivity calculated from the weighted mean of the conductivities (reciprocals of the resistivities) of land and seawater, according to the volume ratio. The resistivity of seawater was fixed during the inversions. The initial model was also used as a prior model.

From the responses of the initial model, plotted in Figure 2, we can compare modeled and observed induction arrows. As the initial model specifies a simple uniform Earth with surrounding oceans, the induction arrows are simply pointing to nearby coastlines and the ocean is affecting induction further inland at longer periods. As expected, the following two features are not explained by the initial model: (1) the real arrows to the east of the volcanic front are pointing towards each other at 16 s and (2) the large northward arrows at northeastern sites at 64 and 256 s.

The 3-D inversion uses an Occam's style inversion scheme (Constable et al. 1987). The model was searched so as to minimize model roughness relative to the prior model as well as data misfit, where the root mean square (RMS) is not less than the target RMS value (1.0 in this study). The selection of model is performed on an RMS basis. In this inversion, a first-generation best model was found after several iterations, using the initial model described above. Then, the best model was used as the initial model, and as the prior model for the series of iterations in the next generation. In this way, we obtained a final resistivity model from the inversion of the third generation with an RMS of 1.4. The final model explains major features of the observed responses, in particular, the two features mentioned previously (directions of arrows to the east of the volcanic front and the large northward arrows at northeastern sites).

Results and discussion

Figure 4 shows representative depth sections of the final model. Figure 4a shows the upper crustal feature of the model. The short-period induction arrows require conductors C1 to C4, the geometry of which implies that they are sedimentary layers. In particular, C1, which runs in a N-S direction to the east of the volcanic front, is responsible for the pairs of arrows pointing towards each other at the period of 16 s. Conductors C2 and C3 likely represent thick Miocene marine sedimentary layers (Sato 1994), and C4 presumably represents Paleozoic sedimentary layers which lie between two resistive regions (R2 and R3) of Cretaceous granitic intrusions (Finn 1994; Ogawa 1992). Conductor C5 is evident at the eastern coast at a depth of 10 km. This conductor is required to explain the large northward induction arrows at sites to the south of C5; however, the implications of the anomaly remain unknown. The anomaly outside of the observed array requires further investigation. A conductor is present below the volcanic zone centered in the Sengan area, located at a depth of 20 km (Figure 1). Figure 4d shows a depth section of the Moho in this area. Conductor C6 spreads in a N-S direction along the volcanic area.

Figure 5 shows resistivity sections for the six profiles in Figure 1. The arrows at the surface represent the location of the backbone range. The Conrad and Moho discontinuities are drawn with broken lines.

The upper crustal conductors (C2 and C3), which are observed on the Japan Sea side as deep as 10 km, can be interpreted as Miocene marine sedimentary layers, dating to the rifting of the Japan Sea (Sato 1994). Conductors C1 and C4 are shallow features (depths of *ca.* 2 km), probably representing Paleozoic sediments in the Kitakami Mountains and presumably separated by resistive granitoids. Conductor C5 is a notable feature, but its implications are not clear, as it is outside of the coverage area of the study.

The distributions of lower crustal conductors are observed from north to south in the depth sections. Conductor C6 is evident in the southern four profiles. The distribution of conductor C6 and its resistivity (1 to 10 Ωm) are also consistent with the results of previous studies (Ogawa et al. 1986; Ogawa 1987b). Recent wideband magnetotelluric profile measurements with site spacings of several kilometers have yielded more detailed images of the locations and depths of these conductors, although those images were limited to two-dimensions (Mitsuhata et al. 2001; Ogawa et al. 2001; Umeda et al. 2006; Mishina 2009; Asamori et al. 2010; Ichihara et al. 2011).

The distribution of the N-S trending regional conductor C6 is consistent with a zone of low P-wave velocity (Vp), low S-wave velocity (Vs), and a high Vp/Vs ratio, as inferred from seismic tomography results (Nakajima et al. 2001a). This low-velocity and high-Vp/Vs zone is located in the upper part of a sheet-like low-velocity zone inclined and parallel with the slab in a mantle wedge (Nakajima et al. 2001b). The inclined sheet-like low-velocity zone is considered to represent the hot upwelling flow of mantle material accompanying subduction, which is partially molten because of the addition of water emanating from the deeper parts of the subducting slab (Hasegawa and Nakajima 2004; Hasegawa et al. 2005). Since this inclined low-velocity zone reaches the Moho beneath the volcanic front, it has been proposed that partially molten materials repeatedly intruded the crust and formed volcanoes (Hasegawa and Nakajima 2004).

In our 3-D resistivity model, an inclined low-resistivity structure is not observed because the depth of our investigation is *ca.* 80 km, at most. The low resistivity is

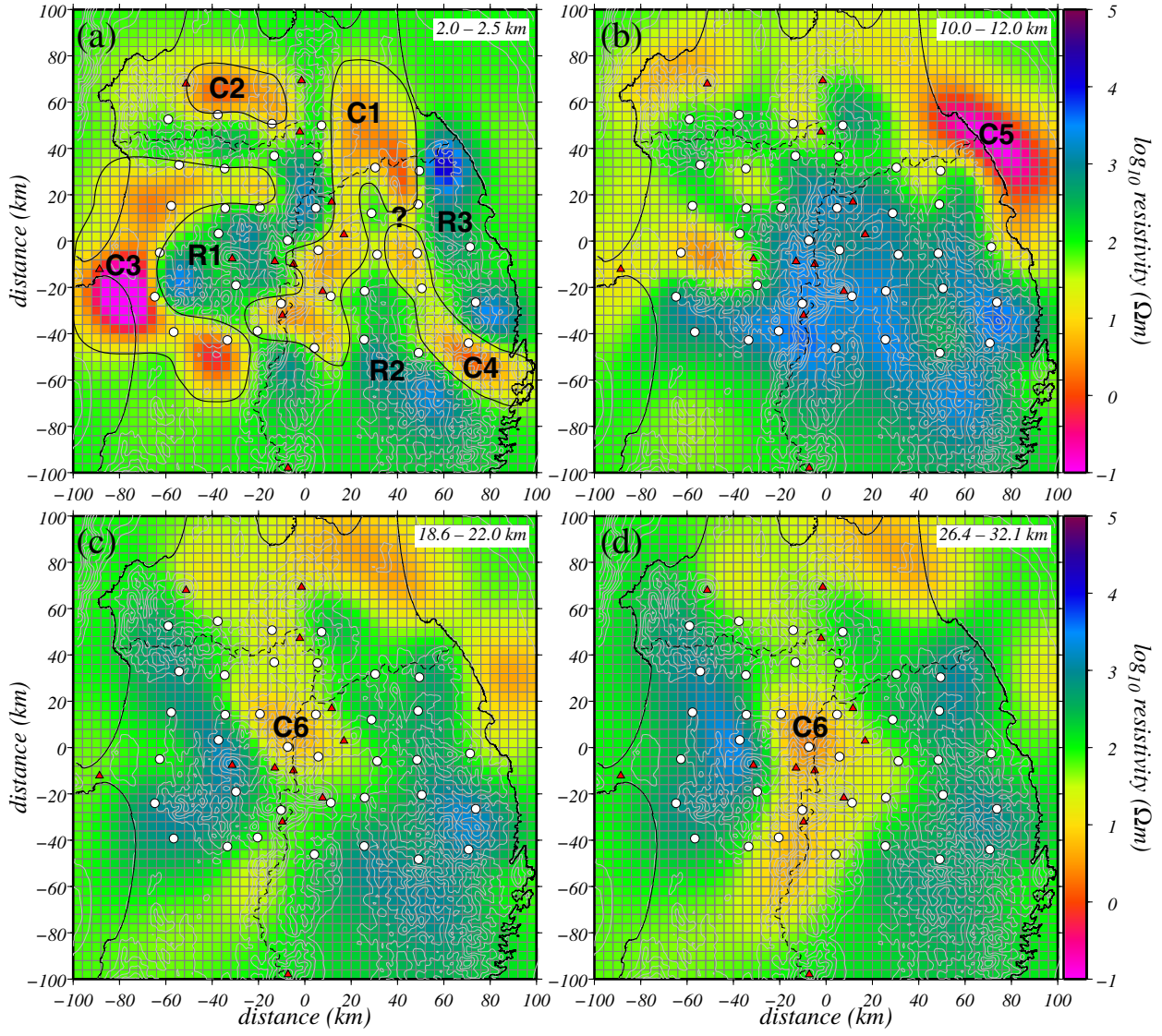

Figure 4 Depth sections of the final 3-D model. Sections at depths of **(a)** 2.0 to 2.5 km, **(b)** 10.0 to 12.0 km, **(c)** 18.6 to 22.0 km, and **(d)** 26.4 to 32.1 km are shown. Red triangles indicate the locations of major quaternary volcanoes (Figure 1); white dots denote observation sites.

continuously distributed from the uppermost mantle to the lower crust along the backbone range, which is not contradictory to the abovementioned seismological images of a volcano generation model. This suggests that the regional conductor inferred beneath the backbone range can be interpreted as arc magma or high-salinity fluids (Kawamoto et al. 2012).

Hasegawa and Nakajima (2004) also proposed a model of volcano generation on the back-arc side. They suggested that upper mantle melt has an along-arc variation, with 'hot fingers' extending upwards beneath the volcanoes. The conductor visible in our 3-D model under the Sengan region (C6) corresponds to one such finger. However, no conductive region is found in the back-arc side, except that the regional conductor C6 seems to extend towards the Iwaki volcano (IWK in Figure 1). We presume that a conductive region was not resolved by the tipper inversion because of the presence of a small-scale structure in either the deep crust or uppermost mantle. Future 3-D magnetotelluric studies will confirm and provide details of such melt/fluid distributions under the volcanoes.

Conclusion

We applied a 3-D inversion to magnetic transfer function data from 37 sites, as presented by Ogawa (1987a). Starting from a 100-Ωm uniform Earth with a fixed resistivity

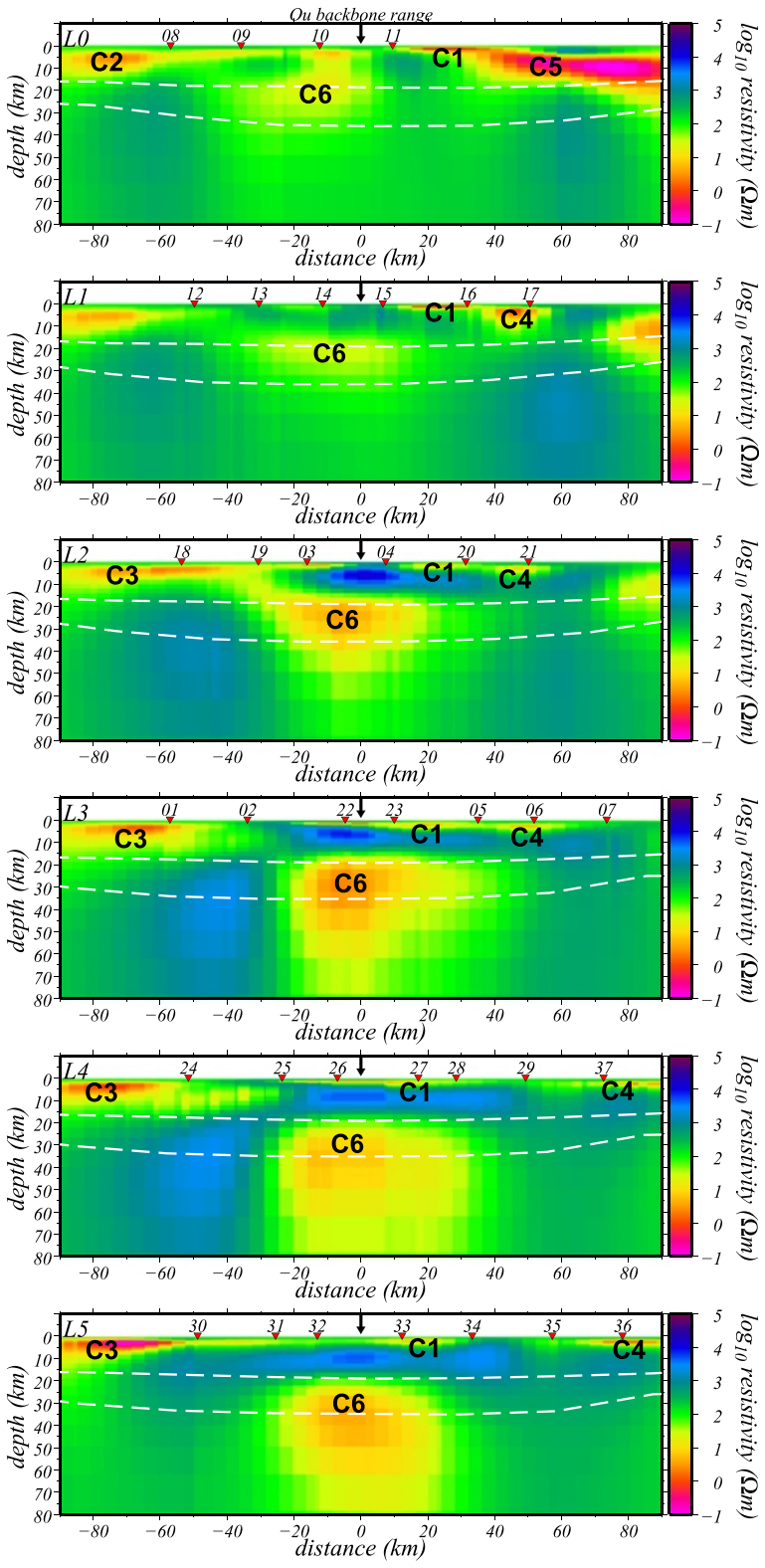

Figure 5 The six E-W cross sections of the final model (L0-L5 in Figure 1). The arrow shows the location of the backbone range and indicates the origin of the horizontal axis. The white dashed lines indicate the Conrad and Moho seismic discontinuities, following Zhao et al. (1994).

structure and a surrounding ocean, the inverted resistivity model showed the following features.

1. Observed induction arrows cannot be accounted for solely by the effect of a conductive ocean enclosing a homogeneously resistive Earth. The ocean effects are particularly small at a period of 16 s.
2. The NTCB, previously inferred from pairs of induction arrows pointing towards each other at a period of 16 s, is attributed to a shallow conductor (C1) located east of the volcanic front. Upper crustal conductors (C2, C3) are required to explain the short period data. We also found a NW-SE trending conductive belt (C4) in the Kitakami Mountains.
3. A N-S trending conductor is located along the volcanic arc in the lower crust. The conductor shallows under the Sengan geothermal area, which is consistent with the results of seismological imaging. This conductor implies a magmatic melt and/or a high-salinity fluid.

Competing interests
The authors declare that they have no competing interests.

Authors' contributions
WK constructed the 3-D conductivity models and drafted the manuscript. YO conceived of the study and revised the manuscript. Both authors read and approved the final manuscript.

Acknowledgements
The authors thank Weerachai Siripunvaraporn of Mahidol University for the use of the inversion program WSINVMT3D (Siripunvaraporn and Egbert, 2009). Constructive comments and suggestions from two anonymous referees were most helpful in improving the manuscript. Numerical calculations were carried out on TSUBAME2.0 at the Global Scientific Information and Computing Center of Tokyo Institute of Technology. Figures were prepared using the Generic Mapping Tools (Wessel and Smith 1991). This study was supported by JSPS KAKENHI Grant Number 21109003.

Received: 15 January 2014 Accepted: 12 May 2014
Published: 27 May 2014

References
Asamori K, Umeda K, Ogawa Y, Oikawa T (2010) Electrical resistivity structure and helium isotopes around Naruko Volcano, Northeastern Japan and its implication for the distribution of crustal magma. Int J Geophys 2010:1–7, doi:10.1155/2010/738139

Avdeev DB, Ogawa Y, Kuvshinov AV, Pankratov OV (1995) An interpretation of magnetovariational data in the northern Tohoku district, Japan, using multi sheet modeling. J Geomag Geoelectr 47:405–410

Constable SC, Parker RL, Constable CG (1987) Occam's inversion: a practical algorithm for generating smooth models from electromagnetic sounding data. Geophysics 52:289–300

Finn C (1994) Aeromagnetic evidence for a buried Early Cretaceous magmatic arc, northeast Japan. J Geophys Res 99:22165–22185, doi:10.1029/94JB00855

Hasegawa A, Nakajima J (2004) Geophysical constraints on slab subduction and arc magmatism. AGU Geophys Monogr 150 IUGG vol 19:81–94

Hasegawa A, Nakajima J, Umino N, Miura S (2005) Deep structure of the northeastern Japan arc and its implications for crustal deformation and shallow seismic activity. Tectonophysics 403:59–75, doi:10.1016/j.tecto.2005.03.018

Honkura Y (1974) Electrical conductivity anomalies beneath the Japan arc. J Geomag Geoelectr 26:147–171

Ichihara H, Uyeshima M, Sakanaka S, Ogawa T, Mishina M, Ogawa Y, Nishitani T, Yamaya Y, Watanabe A, Morita Y, Yoshimura R, Usui Y (2011) A fault-zone conductor beneath a compressional inversion zone, northeastern Honshu, Japan. Geophys Res Lett 38:38–41, doi:10.1029/2011GL047382

Kato Y, Daguchi M, Seto M, Aruga T (1971) Northeastern Japan anomaly of the upper mantle. Sci Rep Tohoku Univ Ser 5 Geophysics 21:19–35

Kawamoto T, Kanzaki M, Mibe K, Matsukage KN, Ono S (2012) Separation of supercritical slab-fluids to form aqueous fluid and melt components in subduction zone magmatism. Proc Natl Acad Sci U S A 109:18695–18700, doi:10.1073/pnas.1207687109

Mishina M (2009) Distribution of crustal fluids in Northeast Japan as inferred from resistivity surveys. Gondwana Res 16:563–571, doi:10.1016/j.gr.2009.02.005

Mitsuhata Y, Ogawa Y, Mishina M, Kono T, Yokokura T, Uchida T (2001) Electromagnetic heterogeneity of the seismogenic region of 1962 M6.5 Northern Miyagi Earthquake, northeastern Japan. Geophys Res Lett 28:4371–4374

Nakajima J, Matsuzawa T, Hasegawa A (2001a) Seismic imaging of arc magma and fluids under the central part of northeastern Japan. Tectonophysics 341:1–17

Nakajima J, Matsuzawa T, Hasegawa A, Zhao D (2001b) Three-dimensional structure of Vp, Vs, and Vp/Vs beneath northeastern Japan: implications for arc magmatism and fluids. J Geophys Res 106:843–857

Nishida Y (1976) Conductivity anomalies in the southern half of Hokkaido, Japan. J Geomag Geoelectr 28:375–394

Ogawa Y (1987a) Preliminary interpretation on detailed magnetovariational profiling in the northern Tohoku district. J Geomag Geoelectr 39:559–569

Ogawa Y (1987b) Two-dimensional resistivity modelling based on regional magnetotelluric survey in the northern Tohoku district, northeastern Japan. J Geomagn Geoelectr 39:349–366

Ogawa Y (1992) Deep crustal resistivity structure revealed by wideband magnetotellurics—Tohoku and Hokkaido region, PhD Thesis. University of Tokyo

Ogawa Y, Yukutake T, Utada H (1986) Two-dimensional modelling of resistivity structure beneath the Tohoku district, northern Honshu Japan, by a finite element method. J Geomagn Geoelectr 38:45–79

Ogawa Y, Mishina M, Goto T, Satoh H, Oshiman N, Kasaya T, Takahashi Y, Nishitani T, Sakanaka S, Uyeshima M, Takahashi Y, Honkura Y, Matsushima M (2001) Magnetotelluric imaging of fluids in intraplate earthquake zones, NE Japan back arc. Geophys Res Lett 28:3741–3744

Parkinson WD (1962) The influence of continents and oceans on geomagnetic variations. Geophys J R Astron Soc 6:441–449

Rikitake T, Yokoyama I (1953) Anomalous relations between H and Z components of transient geomagnetic variations. J Geomag Geoelec 5:59–65

Sato H (1994) The relationship between Late Cenozoic tectonic events and stress field and basin development in northeast Japan. J Geophys Res 99:22261–22274

Schmucker U (1970) Anomalies of geomagnetic variations in the southwestern United States. Bull Scripps Inst Oceanogr 13:165

Simpson F, Bahr K (2005) Practical magnetotellurics. Cambridge University Press, Cambridge, 33

Siripunvaraporn W, Egbert G (2009) WSINV3DMT: vertical magnetic field transfer function inversion and parallel implementation. Phys Earth Planet Interiors 173:317–329

Umeda K, Asamori K, Negi T, Ogawa Y (2006) Magnetotelluric imaging of crustal magma storage beneath the Mesozoic crystalline mountains in a nonvolcanic region, northeast Japan. Geochemistry Geophys Geosystems 7:1–8, doi:10.1029/2006GC001247

Utada H, Hamano Y, Yukutake T (1986) A two-dimensional conductivity model across Central Japan. J Geomagn Geoelectr 38:447–473

Wessel P, Smith WHF (1991) Free software helps map and display data. EOS Trans AGU 72:445–446

Yamashita H, Yokoyama I (1976) Interpretation of the "Northeastern Japan Anomaly" in electrical conductivity of the upper mantle. J Geomag Geoelectr 28:329–332

Zhao D, Hasegawa A, Kanamori H (1994) Deep structure of Japan subduction zone as derived from local, regional, and teleseismic events. J Geophys Res 99:22313–22329

doi:10.1186/1880-5981-66-39
Cite this article as: Kanda and Ogawa: **Three-dimensional electromagnetic imaging of fluids and melts beneath the NE Japan arc revisited by using geomagnetic transfer function data.** *Earth, Planets and Space* 2014 **66**:39.